ACS OMEGA

Open Access

http://pubs.acs.org/journal/acsodf

Article

Interfacial Electronic Interactions within the Pd-CeO_2/Carbon Onions Define the Efficient Electrocatalytic Ethanol Oxidation Reaction in Alkaline Electrolytes

Jimodo J. Ogada,[#] Tobechukwu J. Ehirim,[#] Adewale K. Ipadeola, Aderemi B. Haruna, Patrick V. Mwonga, Aboubakr M. Abdullah, Xiao-Yu Yang, Kamel Eid,* Daniel M. Wamwangi,* and Kenneth I. Ozoemena*

Cite This: *ACS Omega* 2024, 9, 7439−7451

Read Online

ACCESS | Metrics & More | Article Recommendations | Supporting Information

ABSTRACT: Porous Pd-based electrocatalysts are promising materials for alkaline direct ethanol fuel cells (ADEFCs) and ethanol sensors in the development of renewable energy and point-of-contact ethanol sensor test kits for drunk drivers. However, experimental and theoretical investigations of the interfacial interaction among Pd nanocrystals on supports (i.e., carbon black (CB), onion-like carbon (OLC), and CeO_2/OLC) toward ADEFC and ethanol sensors are not yet reported. This is based on the preparation of Pd-CeO_2/OLC nanocrystals by the sol−gel and impregnation methods. Evidently, the porous Pd-CeO_2/OLC significantly increased membrane-free micro-3D-printed ADEFC performance with a high peak power density (P_{max} = 27.15 mW cm^{-2}) that is 1.38- and 7.58-times those of Pd/OLC (19.72 mW cm^{-2}) and Pd/CB (3.59 mW cm^{-2}), besides its excellent stability for 48 h. This is due to the excellent interfacial interaction among Pd, CeO_2, and OLC, evidenced by density functional theory (DFT) simulations that showed a modulated Pd d-band center and facile active oxygenated species formation by the CeO_2 needed for ethanol fuel cells. Similarly, Pd-CeO_2/OLC gives excellent sensitivity (0.00024 mA mM^{-1}) and limit of detection (LoD = 8.7 mM) for ethanol sensing and satisfactory recoveries (89−108%) in commercial alcoholic beverages (i.e., human serum, Amstel beer, and Nederberg Wine). This study shows the excellent possibility of utilizing Pd-CeO_2/OLC for future applications in fuel cells and alcohol sensors.

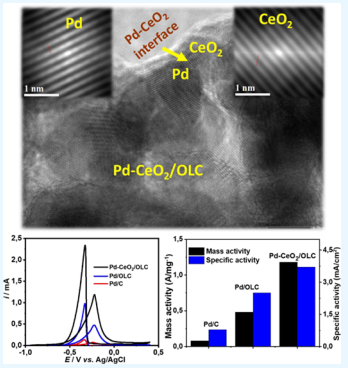

1. INTRODUCTION

Ethanol oxidation reaction (EOR) is an industrially important process intended for the development of ethanol sensors and ethanol fuel cells for electricity generation (a unique technology for the generation of clean and sustainable electricity from ethanol and air).[1] Efficient EOR can find applications in the development of alkaline direct ethanol fuel cells (ADEFCs) which represent one of the most preferable electrochemical energy devices for the development of renewable and clean electricity.[2] The ADEFC has become important because of the impressive properties of ethanol, including its high theoretical energy density, affordability, easy transportation/storage, and nontoxicity.[3] Moreover, large quantities of ethanol are produced from agricultural products and organic municipal wastes; 90 million liters of ethanol are produced globally from agricultural and organic domestic wastes every year.[3]

Electrocatalytic detection or sensing of ethanol is important for a plethora of applications, including in the pharmaceutical industry and the beverage industry and in mitigating the challenges of alcohol abuse and drunk driving in the society. Conventionally, ethanol is determined using a hydrometer, which is fraught with inaccuracies and human errors during reading. Other methods include the use of spectroscopy,[4] and chromatography,[5] which are bulky, expensive, complex, and difficult to miniaturize. Electrochemical techniques, on the other hand, are getting more attention due to their simplicity, accuracy, low cost, and ease of miniaturizing the sensor for use by nonskilled workers.[6]

Palladium(Pd)-based electrocatalysts are one of the most important electrocatalytic materials for alkaline EOR due to the high compatibility of Pd with earth-abundant non-noble metals and excellent activity, whereas the non-noble-metals can also be steady and function sufficiently for electrochemical applications.[7,8] Like other auxiliary metal oxides (such as SnO_2, Mn_3O_4, Co_3O_4, and NiO), CeO_2 is believed to raise the concentration of the surface adsorbed hydroxyl species (OH_{ads}) on the Pd active sites, thereby enabling the C−C bond cleavage and the formation of final EOR products.

Received: June 21, 2023
Revised: September 24, 2023
Accepted: September 27, 2023
Published: February 9, 2024

However, unlike other auxiliary metal oxides, the CeO_2 has been found to endow unique properties toward Pd catalysts: aside from having superior storage capacity for oxygen, it exhibits the Ce^{4+}/Ce^{3+} redox couple during the redox processes that lead to complex Pd−CeO_2 interactions that yield different Pd species.

A noble metal such as Pt or Pd interacts with CeO_2, forming a highly dispersed noble metal ionic catalyst (NMIC) represented as $Ce_{1-x}M_xO_{2-\delta}$ (where M = noble metal, creating oxygen vacancies) rather than existing as metal nanoparticles on CeO_2 support. The $Ce_{1-x}M_xO_{2-\delta}$ is found to be a better electrocatalyst than the same amount of M, attributable to electronic interaction between metal (M) ions and CeO_2 lattice.[9] The existence of the noble metal in the CeO_2 lattice creates the adsorption active sites for the electrocatalytic activities. In other words, for example, the Pd ions act as the adsorption active sites for the electron donating molecule, thereby increasing the EOR kinetics. The synergistic interaction between the noble metal and Ce ions allows for increased electron exchange, resulting in enhanced electrocatalytic activity.[10] However, both Ce and Pd take part in the electrocatalytic process by the synergistic electron transport between them. For example, XPS data had provided some evidence that the interaction of Pd^{2+}/Pd^0 and Ce^{4+}/Ce^{3+} redox couples keeps Pd in its ionic state and, at the same time, permitted the availability of the lattice oxygen for the oxidation reaction.[11] For example, Pd-CeO_2/OLC is an efficient electrocatalyst for the fabrication of durable anion-exchange membrane fuel cells (AEMFC) compared to Pd alone (i.e., Pd-supported on carbon black (Pd/CB), or onion-like carbon (Pd/OLC)) and Pd-CeO_2/CB.[12] In the previous work,[12] the superior performance of the OLC and the ability of CeO_2 to modulate the electronic properties of the Pd were reported. However, the performance of Pd-CeO_2/OLC for ADEFC and the ethanol sensor is yet to be reported, as far as we found.

Herein, porous Pd nanocrystal-anchored CeO_2/OLC support (Pd-CeO_2/OLC) was synthesized by sol−gel, and impregnation methods. This is based on the initial formation of the OLC from the pyrolysis of diamond, followed by the incorporation of CeO_2 into the as-obtained OLC to form the CeO_2/OLC support by sol−gel and then Pd impregnation to form Pd-CeO_2/OLC nanostructures. The fabrication process involves the utilization of the reducing power of ethanol to reduce the Pd precursor and promote its growth on CeO_2/OLC in the formation of Pd-CeO_2/OLC nanostructures. The interfacial interaction among the Pd, CeO_2, and OLC was probed by surface and bulk characterization techniques, which show that Pd-CeO_2/OLC exhibits imitable physicochemical merits, such as porosity (0.23 cm^3/g), surface area (373.53 m^2g), modulated d-band center, lattice strain, and ease of formation of oxygenated species. Similarly, the density functional theory (DFT) studies reveal weak adsorption of the intermediates (CH_3CO* and OH*) and excellent conductivity (low band gap) arising from the highly effective charge of the defect-rich $Ce_{1-x}Pd_xO_{2-\delta}$ and OLC. Thus, the advantages of the interfacial interaction among Pd, CeO_2, and OLC in Pd-CeO_2/OLC for ADEFC and ethanol sensors were demonstrated and compared with Pd/OLC and Pd/carbon black (Pd/CB) in KOH medium.

2. EXPERIMENTAL SECTION

2.1. Materials/Reagents. Acetylene carbon black (TIMICAL SUPER CB, 45 m^2/g, bought from Gelon, China), $PdCl_2$ (≥99.99%), ethylene glycol (EG, 99.8%), ethanol (EtOH ≥ 99.99%), $Ce(NO_3)_3{\cdot}6H_2O$ (99.9%), hydrochloric acid (HCl, 37%) and all other analytical reagents were bought from Sigma-Aldrich without additional purification.

2.2. Preparation Methods. The synthesis methods follow similar approaches previously reported,[13] with modification of different supports (i.e., OLC and CeO_2/OLC).

2.2.1. Preparation of Pd/CB. Pd/CB was prepared by sonicating a mixture of CB (0.25 g), EG (50 mL), H_2O (2.08 mL), $PdCl_2$ (0.042 mg), and HCl (0.25 mL) for 20 min, magnetically stirred in a N_2 flow, and then the addition of NaOH (5.6 mM) to raise the pH to 12 and stirred for 1 h. The resulting mixture was washed with ultrapure H_2O severally until pH 7 and dried at 40 °C in a vacuum oven for 24 h. The dried powder was then heated at 125 °C in a N_2 flow for 3 h and cooled to 25 °C.

2.2.2. Preparation of CeO_2/OLC Support. The OLC was prepared from the annealing of high-purity nanodiamond (98−99%, NaBond Technologies Co.) at high temperature (1300 °C) for 3 h in an Ar flow.[14] CeO_2/OLC was synthesized by sonicating a mixture of the OLC (2.0 g), $Ce(NO_3)_3{\cdot}6H_2O$ (5.05 g) and H_2O (125 mL), then the addition of KOH to raise the pH to 12 and stirred for 3 h. The mixture was washed with ultrapure H_2O severally until a pH of 7 and dried in a vacuum oven at 65 °C for 24 h. The dried powder was then heated to 250 °C in air for 2 h and cooled to 25 °C.

2.2.3. Preparation of Pd-CeO_2/OLC. Pd-CeO_2/OLC was synthesized by magnetically stirring a mixture of OLC-CeO_2 (0.50 g), H_2O (70 mL), ethanol (50 mL), and K_2PdCl_4 (172.5 mg) for 1.5 h and sonicated for 0.33 h, and then the addition of KOH to raise the pH to 12. The mixture was heated at 80 °C for 1 h, cooled to 25 °C, and washed with ultrapure H_2O severally until pH 7 and dried in a vacuum oven at 65 °C for 24 h.

2.3. Physical Characterization. The Pd-CeO_2/OLC and other catalysts were characterized utilizing powder X-ray diffraction (XRD, Bruker D2 Phaser X-ray diffractometer equipped with a Cu−K_α X-rays (λ = 1.5406 Å)) to investigate their crystalline phases. X-ray photoelectron spectroscopy (XPS) gives information about the chemical state of the electrocatalysts. Elemental analysis was conducted with energy-dispersive X-ray spectroscopy (EDX, unit "FEI Nova Nanolab 600 SEM" connected to a scanning electron microscope (SEM)), to establish the chemical compositions and elemental distribution at the electrocatalysts. Transmission electron microscopy (TEM) and its high resolution are acquired from (HRTEM, JEOL 2010F) to obtain information on the structural properties and lattice fringes of the electrocatalysts. Brunauer−Emmett−Teller (BET) analysis was done on the Micromeritics TriStar II 3000 area and porosity analyzer instrument to probe the specific surface areas, porosity, and pore size of the electrocatalysts. Raman spectroscopy was carried out on a Bruker Senterra laser Raman spectrometer to verify the bond vibration of the electrocatalysts.

2.3.1. DFT. The DFT studies were performed with the supercomputational facilities at the Centre for High Performance Computing (CHPC, Cape Town, South Africa), utilizing the BIOVIA Material Studio and employing the adsorption locator tool module. CH_3CO* and *OH molecules served as adsorbates and were adsorbed onto the modeled electrocatalyst's surfaces (i.e., Pd/C, Pd/OLC, and Pd/CeO_2/OLC). Supercells of 3 × 3 were modeled for all the above electrocatalysts. A Material studio cleaning tool was used,

https://doi.org/10.1021/acsomega.3c04427
ACS Omega 2024, 9, 7439−7451

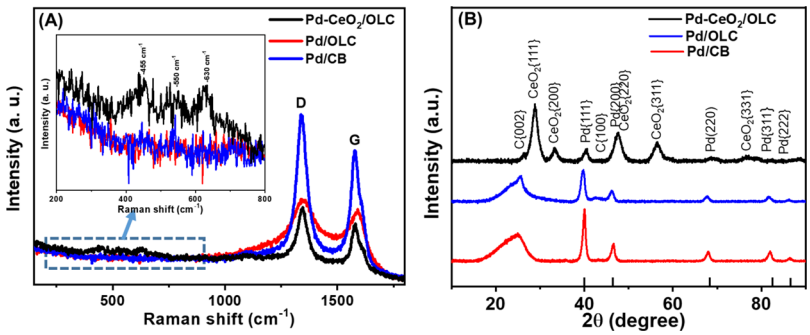

Figure 1. (A) Raman spectra and (B) XRD of Pd-CeO_2/OLC and other electrocatalysts.

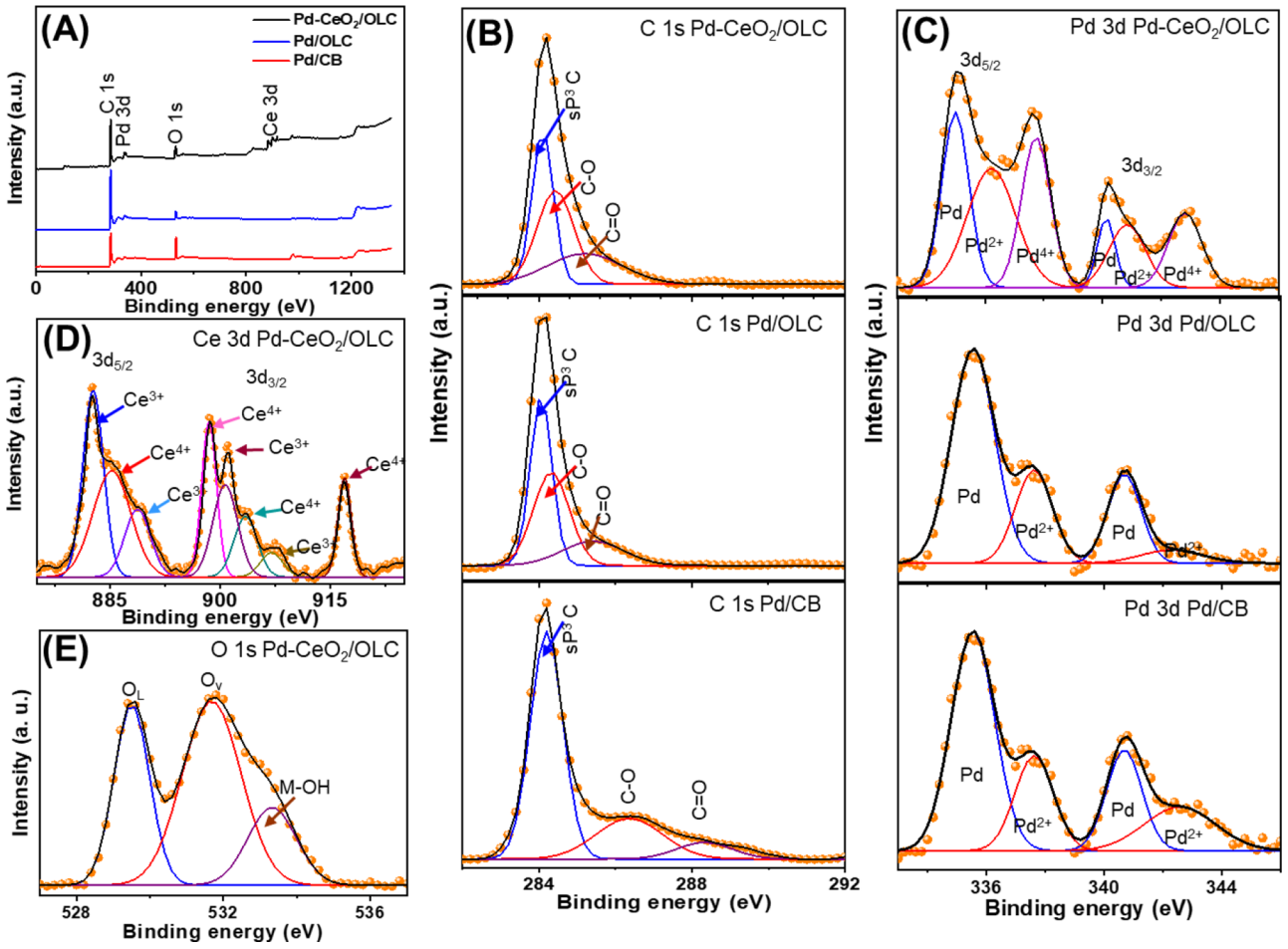

Figure 2. (A) XPS wide spectra, high-resolution XPS of (B) C 1s, (C) Pd 3d, (D) Ce 3d, and (E) O 1s of Pd-CeO_2/OLC and other electrocatalysts.

followed by geometric relaxation calculations with a set threshold energy at 10^{-6} eV for convergence. The lowest adsorption distance was set at 5 Å. DMol^3, another module of the BIOVIA Materials Studio, was used to calculate the electronic properties. The same threshold energy as that utilized for adsorption was set for the calculations of electronic and energy properties. Condensed-phase optimization molecular potential for atomistic simulation studies (COMPASS) force field was used since it guarantees reliable theoretical outcomes.

2.3.2. Electrochemical Measurement. The electrochemical measurements of the electroacatalysts were obtained using an SP300 Bio-Logic Potentiostat operating on EC-Lab software. A three-electrode fashion was utilized for half-cell tests, consisting of a glassy carbon electrode (GCE, diameter (3.0 mm), area (0.0707 cm^2)) modified with the electrocatalyst ink as the working electrode, a platinum wire as the counter electrode (to generate applied potentials at the working electrode), and an AglAgCl electrode (3 M KCl) as the reference (to monitor current generated at the working electrode). The GCE was previously cleaned by proper polishing on a pad using an alumina (Al_2O_3; nanopowder Aldrich) slurry followed by sonication in ethanol and acetone. Each electrocatalyst's ink was prepared by sonicating a mixture of each powder (1 mg), EtOH (1 mL), and Nafion (5 wt %, 100 μL) for 0.5 h to obtain a uniform mixture. Each

https://doi.org/10.1021/acsomega.3c04427
ACS Omega 2024, 9, 7439−7451

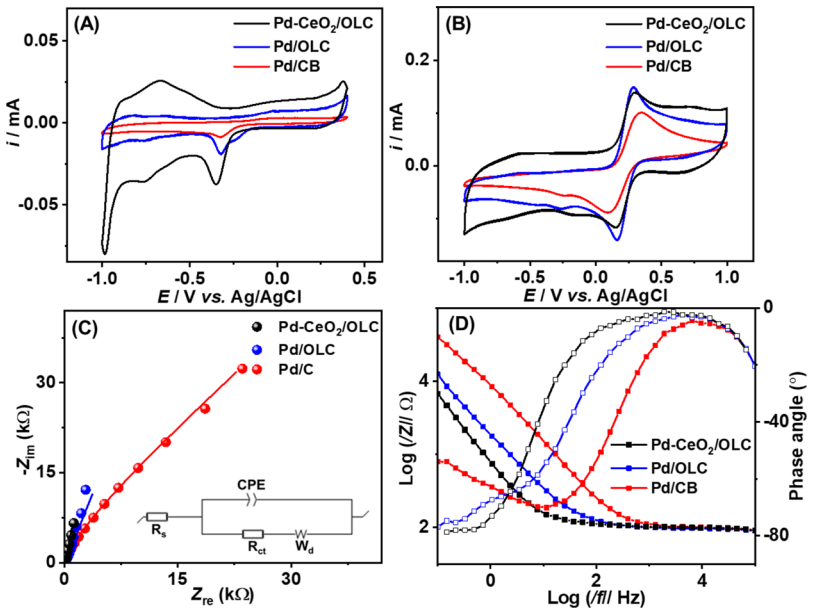

Figure 3. CVs of the Pd-CeO_2/OLC and other electrocatalysts in (A) 1.0 M KOH at 20 mV/s, (B) 3 mM $[Fe(CN)_6]^{4-}/[Fe(CN)_6]^{3-}$ in 0.1 M KCl at 100 mV/s, (C) Nyquist plots and (D) Bode plots in the redox probe solution at the $E_{1/2}$ = 0.22 V (vs AglAgCl). The inset in (C) is Randles' electrical equivalent circuit (EEC) used in fitting the EIS.

electrocatalyst's ink (12 μL) was cast on the GCE and dried, resulting in an electrocatalyst loading (0.0144 mg/cm^2). Electrochemical impedance spectroscopy (EIS) was done at a frequency range (100 kHz and 0.01 Hz) and amplitude (10 mV) in the redox probe (i.e., 3 mM $K_4Fe(CN)_6/K_3Fe(CN)_6$ (1:1 mol ratio) dissolved in 0.1 M KCl). The EIS was performed at an equilibrium potential ($E_{1/2}$) of the redox probe (0.33 V vs AglAgCl) observed from cyclic voltammetry. Alcoholic drinks used for ethanol sensor testing were purchased from local suppliers.

3. RESULTS AND DISCUSSION

3.1. Physical Characterization. The Raman spectra of the Pd-CeO_2/OLC, Pd/OLC, and Pd/CB show the two characteristic peaks of carbons around 1360 cm^{-1} (d-band, describing the degree of defect or disorder in carbon, i.e., sp^3-bonded carbon atoms) and ~1590 cm^{-1} (g band, describing the degree of graphitization in carbon, i.e., sp^2-bonded carbon atoms) (Figure 1A). A similar observation was reported elsewhere.[15] The ratio of the bands (I_D/I_G) follow an incremental trend of Pd-CeO_2/OLC (1.35) > Pd/OLC (1.26) > Pd/CB (1.01), implying that incorporation of CeO_2 in Pd-CeO_2/OLC. Moreover, the Pd-CeO_2/OLC shows weak bands at ~630 cm^{-1} assigned to the longitudinal optical (LO) mode of CeO_2,[16] and is evident of vacancies of oxygen (O_v) in the CeO_2 lattice.[16] The weakness of this band suggests the presence of a high number of O_v (i.e., Pd−$Ce_{1-x}O_{2-y}$/OLC). Indeed, the weak and broad bands at ~550 and ~450 cm^{-1} are clear indications of defects or disordering as well as increased Pd−O−Ce bond strength.[17] The absence of bands below 400 cm^{-1} is due to a decrease in the crystallite size.[17] In general, one can conclude that Pd/CeO_2−OLC is made up of small nanocrystal sizes.

The XRD patterns of the electrocatalysts show a significant {002} for the amorphous graphitic carbon structure in Pd/CB and Pd/OLC, but a weak peak in Pd-CeO_2/OLC (Figure 1B). The suppression of C(002) in Pd-CeO_2/OLC is due to the high intensity of the adjacent CeO_2. All the catalysts have diffraction patterns of (111), (200), (220), (311), and (222) assigned to the facets of face-centered cubic (*fcc*) of Pd crystals, in addition to (111), (200), (220), (311), and (331) facets of CeO_2 only in Pd-CeO_2/OLC. However, the lower intensity and full-width half-maximum (fwhm) of (111) facet of Pd in Pd-CeO_2/OLC (fwhm = 0.39) than in Pd/OLC (0.89) and Pd/CB (0.45), is an indication of the electronic interaction of CeO_2 with Pd/OLC. This also led to the predominant higher facet of Pd (i.e., (220)) relative to the usual lower facet of Pd (i.e., (111)) of the Pd-CeO_2/OLC. Similarly, the Pd diffraction pattern of Pd-CeO_2/OLC shifted to higher 2θ compared to Pd/OLC and Pd/CB, implying lattice contraction of Pd after the incorporation of CeO_2. This is due to the excellent interfacial interaction in Pd-CeO_2/OLC, evidenced by the reduced lattice constant of Pd (0.86 Å), which is beneficial for electrocatalysis.[18]

The XPS of the Pd-CeO_2/OLC, Pd/OLC, and Pd/CB show the wide surveys of core states of Pd 3d/Ce 3d/C 1s/O 1s in Pd-CeO_2/OLC, Pd 3d/C 1s/O 1s in Pd/OLC and Pd 3d/C 1s/O 1s in Pd/CB with respective atomic content of 1.2/1.6/84.6/12.6 at %, 0.6/93.5/5.9 at % and 0.5/79.9/18.1 at % (Figure 2A). The C 1s spectra of the Pd-CeO_2/OLC, Pd/OLC, and Pd/CB show sp^3 C, C−O, and C═O (Figure 2B). The binding energies of C 1s spectra significantly shift negatively in the following trend of Pd-CeO_2/OLC < Pd/OLC < Pd/CB, implying decreased electron density in the carbon matrix by the interfacial interaction of Pd-CeO_2. Figure 3C shows the core Pd 3d spectra deconvolution into Pd^0 ($3d_{5/2}$ and $3d_{3/2}$) and Pd^{2+} ($3d_{5/2}$ and $3d_{3/2}$) as main metallic phase and minor oxide phase, respectively, for the Pd-CeO_2/OLC, Pd/OLC, and Pd/CB. The ratio of Pd^0/Pd^{2+} in Pd-CeO_2/OLC (1.13) is lower than those of Pd/OLC (1.18) and Pd/CB (1.24), which reveals Pd oxide is more abundant in the Pd-CeO_2/OLC. This is further corroborated by an additional peak of Pd^{4+}($3d_{5/2}$ and $3d_{3/2}$) in the Pd 3d of Pd-CeO_2/OLC, due to the interfacial interaction of with CeO_2 to form a stable solid solution (i.e., Ce_{1-x} $Pd_xO_{2-\delta}$). A similar observation was

https://doi.org/10.1021/acsomega.3c04427
ACS Omega 2024, 9, 7439−7451

reported previously.[9,19] Notably, the Pd^0/Pd^{2+} spectra of Pd-CeO_2/OLC shifted to lower binding energies compared to Pd/OLC and Pd/CB, due to the downshifting of the d-band center of Pd by CeO_2, owing to decreased electron density, but improved interfacial interaction for easy desorption of ethanol intermediate species, beneficial for promoting EOR electrocatalysis. The Ce 3d spectra of Pd-CeO_2/OLC were fitted to Ce^{3+} ($3d_{5/2}$ and $3d_{3/2}$) and Ce^{4+} ($3d_{5/2}$ and $3d_{3/2}$) as major and minor oxide phases (Figure 2D). The high intensity of Ce^{3+} is an indication of vacancies of oxygen in the CeO_2 lattice and facilitates improved nanoparticles' dispersion, and is a favorable feature for electrocatalysis.[20] The high-resolution O 1s core-level reveals lattice oxygen (O_L), oxygen vacancies (O_v), and metal-bonded hydroxyl group (M−OH),[21−23] implying that the O is strongly bonded to CeO_2, although with some vacancies and strong oxophilic features, respectively (Figure 2E).

The spherical-like Pd nanoparticle dispersion on the supports (i.e., CeO_2/OLC, OLC, and CB) is revealed by the TEM images (Figure S1A−S1C). The nanoparticle size distribution data, where the average particle increase as Pd-CeO_2/OLC (6.2 nm) < Pd/OLC (7.5 nm) ≪ Pd/C (52 nm) (Figure S1D−S1F). The reduced mean nanoparticle size of Pd-CeO_2/OLC is attributed to the lattice contraction of Pd by the CeO_2. This is further proved by HRTEM, which reveals a lower lattice fringe of 0.226 nm for Pd-CeO_2/OLC than Pd/OLC (0.251 nm) and Pd/CB (0.258 nm) (Figure S1G−S1I). The EDX analysis shows the existence of C, O, Ce, and Pd in Pd-CeO_2/OLC, only C and Pd in Pd/OLC and Pd/CB, with corresponding atomic contents of 55.44/9.81/24.86/9.89 at %, 9.96/90.04 at %, and 10.05/89.95 at % (Figure S2). A single-point BET data of the electrocatalysts shows that their specific surface area (SSA) and porosity decrease as Pd-CeO_2/OLC (373.53 $m^2\ g^{-1}$; 0.230 $cm^3\ g^{-1}$) > Pd/OLC (357.73 $m^2\ g^{-1}$; 0.225 $cm^3\ g^{-1}$) > Pd/CB (35.70 $cm^2\ g^{-1}$; 0.141 $cm^3\ g^{-1}$) (Table S1). However, the pore sizes increase as follows: Pd/CB (15.78 nm) > Pd/OLC (2.53 nm) > Pd-CeO_2/OLC (2.47 nm).

3.2. Cyclic Voltammograms and EIS: Heterogeneous Electron-Transfer Kinetics. First, the cyclic voltammograms (CVs) of all the electrocatalysts in 1.0 M KOH show well-resolved voltammograms with characteristics of hydrogen adsorption/desorption peaks at around −0.6 to −1.0 V (vs Ag/AgCl), small broad Pd oxidation peak around 0.0 V (vs Ag/AgCl), and PdO reduction peak at −0.35 V (vs Ag/AgCl) (Figure 3A). However, the PdO reduction peak of Pd-CeO_2/OLC shifts significantly to a lower potential because the CeO_2/OLC facilitates quick reduction of PdO with a lower energy. Remarkably, the hydrogen underpotential deposition (HUPD) of Pd-CeO_2/OLC is higher than Pd/OLC and Pd/CB, implying increased active sites and electrochemical active surface area (ECSA). Hence, the ECSA of each electrocatalysts is determined from the integration of the HUPD peak, following the established eq 1:

$$\mathrm{ECSA} = \frac{Q}{S.\ I} \tag{1}$$

where Coulombic charge (Q = 0.1507 mC, 0.0551 mC, and 0.0213 mC for Pd-CeO_2/OLC, Pd/OLC, and Pd/CB, respectively), Coulombic constant for monolayer of Pd (S = 0.424 mC cm^{-2}), and electrocatalyst's loading (I = ∼1.0 μg_{Pd}). The ECSA of the Pd-CeO_2/OLC (35.5 m^2/g) is higher than that of Pd/OLC (13.0 $cm^2\ g^{-1}$) and Pd/CB (5.1 $cm^2\ g^{-1}$) by factors of 2.73 and 6.96, respectively, due to the interfacial interaction of Pd and CeO_2.

Second, we sought to investigate the cyclic voltammetric properties of Pd-CeO_2/OLC and other electrocatalysts in the redox probe solution (3 mM $[Fe(CN)_6]^{4-}/[Fe(CN)_6]^{3-}$ in 0.1 M KCl) (Figure 3B). The electrochemical properties of Pd-CeO_2/OLC, Pd/OLC and Pd/CB are summarized in Table 1.

Table 1. Electrochemical Parameters of the Electrocatalysts Obtained from Cyclic Voltammetry Experiments Conducted in the Electrolyte Solution of the Redox Probe (3 mM $[Fe(CN)_6]^{4-}/[Fe(CN)_6]^{3-}$ in 0.1 M KCl)

CV	Pd/CB	Pd/OLC	Pd-CeO_2/OLC
E_{pa}/V	0.347	0.285	0.293
E_{pc}/V	0.089	0.159	0.151
ΔE_p/V	0.258	0.222	0.142
$E_{1/2}$/V	0.220	0.220	0.222
I_{pa}/mA	0.100	0.149	0.138
I_{pc}/mA	−0.088	−0.141	−0.116
I_{pa}/I_{pc}	1.14	1.06	1.19

From the CV data, the electrodes showed perfect reversibility ($I_{pa}/I_{pc} \approx 1$). The electron-transfer kinetics (indicated by the values of the ΔE_p) decreased as Pd-CeO_2/OLC < Pd/OLC < Pd/CB, indicating that Pd-CeO_2/OLC gives the fastest electron transport. Further analysis of the CV curves shows a linear relationship (R^2 > 0.99) between peak current response against square root of the scan rates ($\upsilon^{1/2}$ ($(mV/s)^{1/2}$)) for Pd-CeO_2/OLC, and other electrocatalysts, which confirms a diffusion-controlled process for all in agreement with the Randles-Sevcik theory (Figure S3).

The EIS of the Pd-CeO_2/OLC and other electrocatalysts was utilized to investigate the interfacial interaction. Figure 3C,D represents the fitted Nyquist and Bode plots, respectively. The EIS were successfully fitted with the conventional Randles EEC circuit, comprising electrolyte resistance (R_s), charge-transfer resistance (R_{ct}), and constant phase element (CPE) that describes the electrocatalysts' surface roughness, heterogeneity in surface terminations, porosity, and complexity in the double-layer structure, and Warburg resistance (W_d) (Figure 3C inset). The impedance due to the CPE is defined in eq 2:[24,25]

$$Z_{\mathrm{CPE}} = \frac{1}{Q(j\omega)^{\beta}} \tag{2}$$

where Q represents the nonideal capacitance ($j = \sqrt{-1}$), ω is the radial frequency, while β is the ideality factor with values −1 and +1 (i.e., $-1 \le \beta \le 1$: when β = 0, Z_{CPE} is an ideal resistor; when β = 1, the Z_{CPE} is the same as the Z_C wherein the interface behaves like an ideal capacitor ($Q = C$); when n = −1, the Z_{CPE} is an ideal inductor; and when β = 0.5, the Z_{CPE} is said to behave as the W_d. The EIS data and kinetics of the electrocatalysts are summarized in Table 2, where R_s values (∼96−97 Ω) are essentially the same, which is expected as the same electrolyte was used for the experiment. The R_{ct} decreases as follows: Pd/CB (15.85 kΩ) > Pd/OLC (2.03 kΩ) > Pd-CeO_2/OLC (0.81 kΩ), implying that electron transfer at the Pd-CeO_2/OLC is about 2.5 and 20 times faster than at the Pd/OLC and Pd/CB, respectively. A similar trend is observed for the W_d values (i.e., Pd/CB ≫ Pd/OLC > Pd-CeO_2/OLC), which means that ionic diffusion is fastest with the Pd-CeO_2/OLC compared to the other catalysts. The β

https://doi.org/10.1021/acsomega.3c04427
ACS Omega 2024, 9, 7439−7451

Table 2. EIS and Kinetics Parameters of the Electrocatalysts Obtained from EIS Experiments Conducted in the Redox Probe Solution (3 mM $[Fe(CN)_6]^{4-}/[Fe(CN)_6]^{3-}$ in 0.1 M KCl)

EIS & kinetic data	Pd/CB	Pd/OLC	Pd-CeO_2/OLC
R_s/Ω	97.10 ± 0.27	96.05 ± 1.23	96.40 ± 0.20
$R_{ct}/k\Omega$	15.85 ± 3.77	2.03 ± 0.95	0.81 ± 0.09
$W_d/k\Omega\ s^{-1/2}$	7.25 ± 0.36	1.73 ± 0.42	0.45 ± 0.54
CPE/$\mu F\ s^{(\beta-1)}$	20.05 ± 0.02	124.30 ± 4.05	246.30 ± 0.08
β	0.84	0.80	0.90
phase angle (°)	−70.4	−75.4	−77.9
knee frequency, $f°$ (Hz)	398.11	37.17	11.22
period, τ (ms)	2.5	27	89
$k_{app}/cm\ s^{-1}$	5.6×10^{-5}	1.1×10^{-4}	2.2×10^{-4}

values are between 0.8 and 0.9, suggesting that all the electrocatalysts exhibit pseudocapacitive behavior (i.e., mixed Faradaic and non-Faradaic properties).

The Bode plots provide some insights into the charge-transport phenomenon. The phase angles are approximately between −70° and −80°, which are less than the ideal −90° for an ideal capacitance, confirming the pseudocapacitive behavior (Figure 3D). The *knee frequency* (aka onset frequency, $f°$, which is defined as the transition point between the high and low frequency components) is highest for the Pd/CB (398.11 Hz, τ = 2.5 ms) compared to the Pd/OLC (37.17 Hz, τ = 27 ms) and Pd-CeO_2/OLC (11.22 Hz, τ = 89 ms). The knee frequency describes the power capability of an ideal double-layer capacitor (which is a pure physical process, non-Faradaic, with no electron transport); the higher the value, the faster the charge−discharge cycle. The Pd-CeO_2/OLC exhibits the lowest frequency, which suggests that it behaves more like a pseudocapacitor (electrochemical process, Faradaic/redox activity) that permits fast electron transport. This is consistent with the R_{ct} data that shows the fastest electron transport for the Pd-CeO_2/OLC. The apparent heterogeneous electron-transfer rate constant (k_{app}) of the electrocatalysts is obtained following eq 3:

$$k_{app} = \frac{RT}{n^2F^2ACR_{ct}} \quad (3)$$

where number of electrons (n = 1) transferred, the Faraday constant (F = 96484.331 C), the ideal gas constant (R = 8.3145 J $mol^{-1}\ K^{-1}$), absolute temperature (T = 298.16 K), experimentally determined area of each electrode (A, cm^2), the R_{ct} (Ω) is obtained from the fitted Nyquist plots, concentration ($C = 3 \times 10^{-6}$ mol cm^{-3}) of the redox probe solution.

Interestingly, the k_{app} for the Pd-CeO_2/OLC (2.3×10^{-4} cm s^{-1}) is about twice larger than that of the Pd/OLC (1.1×10^{-4} cm s^{-1}), while Pd/CB (5.6×10^{-5} cm s^{-1}) is less magnitude than the two OLC-based electrocatalysts. This result is consistent with the R_{ct} and knee frequency data and represents the first detailed physicochemical analysis of an electrocatalyst deployed for EOR.

3.3. Electrocatalytic Alkaline EOR. The behavior of the Pd-CeO_2/OLC and other electrocatalysts toward EOR was implemented in 1 M KOH. Figure 4A shows the CVs of the electrocatalysts in a mixture of 1 M KOH and 1 M ethanol. Two distinct oxidation peaks were recorded, which are the signature of the oxidation of the ethanol to carbonyl species (i.e., the forward or right peak) and the further oxidation of

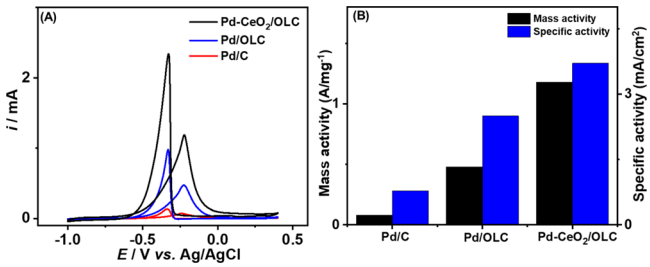

Figure 4. (A) CVs of a mixture of 1 M KOH/1 M ethanol, and (B) mass and specific activities of the Pd-CeO_2/OLC and other electrocatalysts.

adsorbed carbonaceous species to carboxylic acid or carbon dioxide (i.e., reverse or left peak). It is well established that C−C cleavage during EOR on Pd surface is extremely difficult but rather follows the reaction between the adsorbed acetyl group and hydroxyl groups to generate acetic acid as the rate-determining step (rds, eq 4) and subsequently the formation of carboxylic acid as the main product of EOR in alkaline (eq 5):

$$Pd - (CH_3CO)_{ads} + Pd - OH_{ads} \xrightarrow{slow} Pd - CH_3COOH + Pd \quad (4)$$

$$Pd - CH_3COOH + OH^- \xrightarrow{fast} CH_3COO^- + H_2O + Pd \quad (5)$$

The Pd-CeO_2/OLC delivers high mass/specific activities of 1.18 A mg^{-1}/3.71 mA cm^{-2}, which are 2.46/1.48 times that of Pd/OLC (0.48 A mg^{-1}/2.50 mA cm^{-2}) and 14.75/4.76 times that of Pd/CB (0.08 A mg^{-1}/0.78 mA cm^{-2}) (Figure 4B). The improved catalytic activity of Pd-CeO_2/OLC relative to Pd/OLC and Pd/CB may be ascribed to several factors. It is well known that the interatomic interaction of Pd with CeO_2, which is prone to leaching out under electrochemical conditions, results in a surface rich in active noble metal.[26] Also, the interatomic interaction of Pd with CeO_2 tends to change the geometric ligand (i.e., reduced Pd−Pd bond distance) or electronic impact (i.e., modulated d-band center of Pd), so the CeO_2 adjusts the electronic merits of Pd/OLC to yield a more active catalytic surface.[6,12] The EOR activities of the Pd-CeO_2/OLC (1.18 A mg^{-1}/3.71 mA cm^{-2}) are superior to several reports in the literature, including PtPd/RGO (0.6 A mg^{-1}/2.23 mA mg^{-1}),[27] $Pd_{50}Ag_{50}$ (1.97 A mg^{-1}),[28] Au@Pd (1.75 A mg^{-1}/0.77 mA cm^{-2})[29] and Pd NPs@Ni SAC (1.09 A mg^{-1}/1.28 mA cm^{-2})[30] (Table S2).

As can be observed in Figure 4A, the Pd-CeO_2/OLC has an onset potential (−0.68 V) lower than Pd/OLC (−0.57 V) and Pd/CB (−0.46 V), indicating that Pd-CeO_2/OLC requires low energy for the electrooxidation of ethanol.[31] Moreover, the electrocatalysts follow a trend of Pd-CeO_2/OLC > Pd/OLC > Pd/CB with respect to forward current responses of 1.1875, 0.4886, and 0.0773 mA. The increased current response of the Pd-CeO_2/OLC shows that it has the best kinetics for ethanol oxidation among the electrocatalysts studied.

Scan rate studies of the electrocatalysts toward the oxidation ethanol were shown, where the current response increased as the scan rates increased (Figures 5A−C). The plots of the peak forward current response to the square root of the scan rates give a straight line for all the electrocatalysts with regression close to unity, confirming that the interaction of the ethanol onto the electrodes' surfaces is a diffusion-controlled process

https://doi.org/10.1021/acsomega.3c04427
ACS Omega 2024, 9, 7439−7451

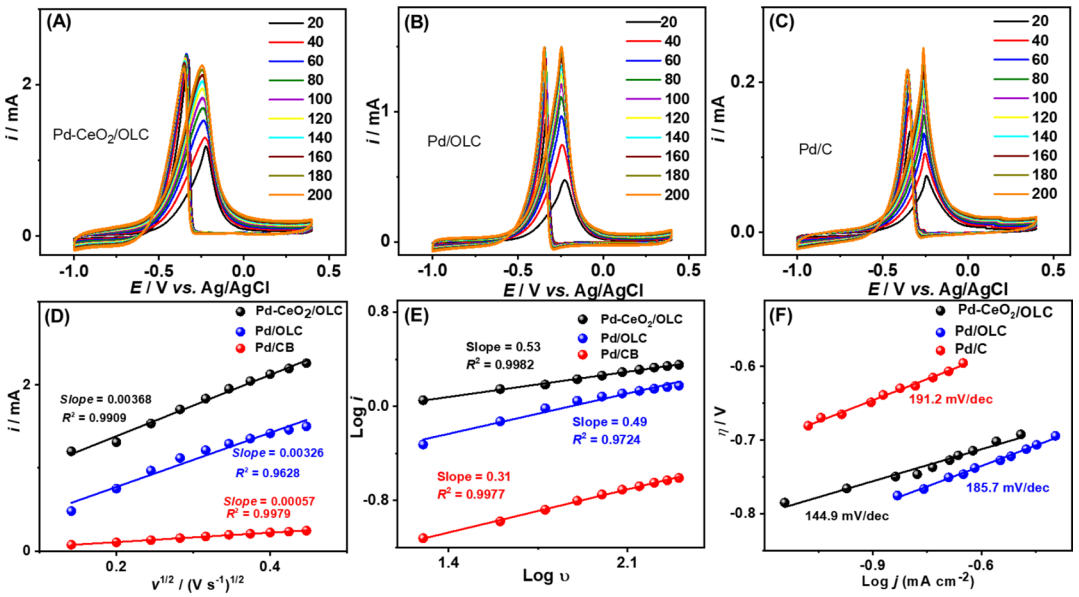

Figure 5. (A–C) Scan rate studies (mV s^{-1}), (D) plots of the peak current versus the square root of scan rates, (E) logarithm of peak current against the logarithm of scan rate, and (F) Tafel plots of the Pd-CeO_2/OLC and other electrocatalysts toward EOR.

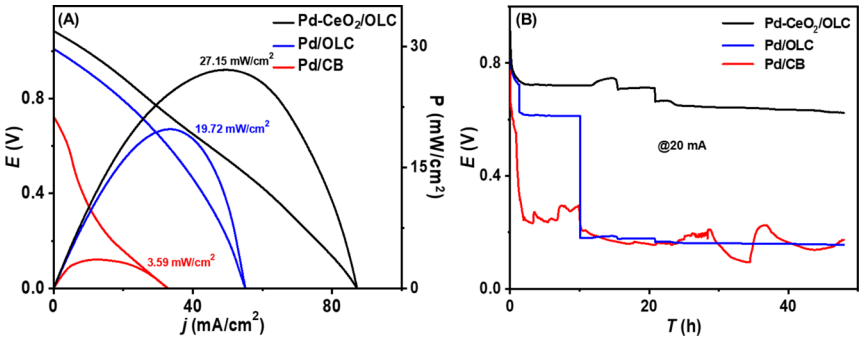

Figure 6. (A) Voltage-power curves and (B) galvanostatic discharge stability test at 20 mA cm^{-2} of the Pd-CeO_2/OLC and other electrocatalysts in a mixture of 2.0 M EtOH/2.0 M KOH solutions.

(Figure 5D), evidenced by the increased slope of Pd-CeO_2/OLC (0.00368) than Pd/OLC (0.00326) and Pd/CB (0.00057), inferring that the ethanol intermediates diffused more rapidly on Pd-CeO_2/OLC. This was further clarified with the logarithmic plot of the forward peak current (Log j_{pf}) vs scan rate (υ / mVs^{-1}) increased linearly with a higher slope for Pd-CeO_2/OLC (0.53) than Pd/OLC (0.49) and Pd/CB (0.31) (Figure 5E). Note that the peak potential of the forward peak (E_{pf}/V) shifts slightly to the positive direction as the scan rate increased; however, the backward peak current did not change with the scan rate, which may suggest an improved tolerance to poisoning from carbonaceous intermediates. Tafel slope is a critical parameter that provides insight into the rate-determining step of the EOR. It is obtained using the conventional Tafel eqs (eqs 6 and 7):

$$\eta = a + b\log j \tag{6}$$

Rearranged as

$$b = \frac{2.303RT}{\alpha nF} \tag{7}$$

where b = Tafel slope, α is the charge-transfer coefficient (assume 0.5), n represents the number of electrons involved in the rds, other terms retain their defined meaning above. The Tafel slopes of the electrocatalysts decrease as Pd/CB (~191 mV dec^{-1}) > Pd/OLC (~ 186 mV dec^{-1}) > Pd-CeO_2/OLC (~145 mV dec^{-1}) (Figure 5F). The values of the Tafel slopes are greater than the expected value of 120 mV/dec for EOR,[32] which suggests that the rds of the EOR is not controlled by just the adsorption of the OH but most likely by other surface reactions that complicate the kinetics. However, since the values obtained in this work are of the same magnitude for the three electrocatalysts, one may conclude that the electrocatalysts have the same reaction mechanism for the EOR, with the Pd-CeO_2/OLC (with the least Tafel slope) providing the fastest electron-transfer kinetics compared to other electrocatalysts.

3.3.1. Performance in Ethanol Micro-Fuel Cell. The fuel cell performance of the Pd-CeO_2/OLC and other electrocatalysts was tested for EOR in a real device, i.e., a membraneless direct ethanol micro-fuel cell (μ-DEFC). Figure 6 compares the voltage-power curves and the corresponding galvanostatic discharge curves for the three Pd-based electrocatalysts. The peak power densities decrease as Pd-CeO_2/OLC (27.15 mW cm^{-2}) > Pd/OLC (19.72 mW cm^{-2}) > Pd/CB (3.59 mW cm^{-2}) (Figure 6A). In addition to delivering the highest peak power density, the Pd-CeO_2/OLC shows excellent voltage retention of ca. 78% (from 0.8 to 0.62 V)

https://doi.org/10.1021/acsomega.3c04427
ACS Omega 2024, 9, 7439−7451

during a 40-h discharge; the Pd/OLC crashed within the first 1.43 h (from 0.8 to 0.62 V) and then at the 10th hour and stabilized at 0.18 V (energy retention of ∼23%), while the Pd/CB crashed within the first 30 min to 0.25 V and then at the 10th hour and stabilized at 0.18 V (energy retention of ∼23%) (Figure 6B). Notably, the morphology of the Pd-CeO_2/OLC, Pd/OLC and Pd/CB did not change after the 48 h long stability, evidenced by the TEM images after the galvanostatic discharge test (Figure S4A−S4C).

3.3.2. Performance in Electrocatalytic Detection of Ethanol. Since the Pd-CeO_2/OLC has the best performance for EOR and ADEFC, additional experiments for the sensing of ethanol and its detection in commercial beer and wine, as well as interferent studies with serum, mimic the condition in humans. The sensing of alcohol on the Pd-CeO_2/OLC electrocatalyst alone was studied using the chronoamperometry (CA) technique. The study was done with a blank (i.e., alkaline electrolyte without the alcohol) and very low concentrations of alcohol (38.5−666.7 mM) (Figure 7A). It

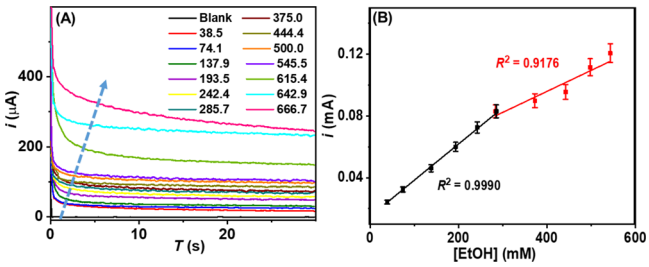

Figure 7. (A) Typical chronoamperometric curves obtained in 1 M KOH containing different ethanol concentrations (0−666.7 mM), and (B) plots peak current response versus concentration of ethanol of Pd-CeO_2/OLC.

was observed that the current response of the chronoamperometry increased with increasing concentrations of the alcohol. Figure 7B shows a plot of peak current (i, μA) at 2.5 s against the ethanol concentrations. The electrode shows satisfactory linearity in the range of 38.5−286 mM, sensitivity (m = 0.00024 mA mM^{-1}), and limit of detection (LoD ∼ 8.7 mM), determined from LoD = 3 s/m, where s is the standard deviation of the blank or y-intercept. The values were calculated as the mean of five experiments.

To demonstrate the possibility of the Pd-CeO_2/OLC as a potential electrocatalyst for the detection of alcohol in real samples, commercial beer (Amstel beer), commercial wine (Nederberg wine), and human serum were tested using the standard addition method. Each sample was tested five consecutive times and quantified using the standard linear plots. Relatively high recoveries (89−108%), were achieved as summarized in Table S3, confirming that the Pd-CeO_2/OLC has the potential to be developed as a viable electrocatalytic sensing platform for a variety of alcohol samples.

3.4. Underlying Science behind the High Performance of the Pd-CeO_2/OLC Electrocatalyst toward EOR. For the theoretical calculation, the {111}[33] facet of Pd was chosen as the electrocatalyst surface's model since it is known to give the highest EOR activity among the low-index surfaces. Also, the choice of the {111} facet of CeO_2 and {002} facet of the OLC originates from their prevalence in the XRD patterns. The acetyl (CH_3CO^*) and hydroxyl (OH^*) species were the adsorbates because it is well-known, both by experiments[34] and theory,[35] that the EOR follows the formation of acetic acid (CH_3COOH) via the oxidation of the adsorbed CH_3CO^* by OH^*,[36] as shown in eq 8:

$$CH_3CO^* + OH^* \rightarrow CH_3COOH^* + * \quad (8)$$

Experimentally, FTIR of the EOR product reveals functional groups of $(-OH)_{Acid}$, $(C{=}O)_{Acid}$, (C−H) stretching, and $(C-O)_{Acid}$ at 3350, 1720, 1470, and 1100 cm^{-1}, respectively implies the formation of acetic acid (Figure S4D).

Figure 8 exemplifies the adsorption of CH_3CO^* on the electrocatalysts' surfaces. The adsorption energy window was set at 100 kcal/mol and minimum energy difference set at 0.0 kcal/mol. In the DFT study, the adsorption energy (E_{ad}, eV) is defined in eq 9:[12,37,38]

$$E_{ad} = (E_{surface+adsorbate}) - (E_{surface} + E_{adsorbate}) \quad (9)$$

where $E_{surface+adsorbate}$ represents the total energy of the interacting catalyst's surface and the adsorbate, while $E_{surface} + E_{adsorbate}$ is the energies of the catalyst's surface and the free adsorbate in the gas phase. This equation reveals that the more negative E_{ad}, the stronger the adsorption. The DFT results (summarized in Table S4) show that the strongest adsorption of CH_3CO^* is observed for the Pd/CB (−25.494 eV) relative to the Pd/OLC (−16.503 eV) and Pd-CeO_2/OLC (−16.811 eV).

The weaker adsorption of CH_3CO^* on the Pd/OLC and Pd-CeO_2/OLC predicts better electrocatalytic conversion of the acetyl to acetic acid on the OLC-based electrodes. The E_{ad} of Pd-CeO_2/OLC is 1.87% higher than that of the Pd/OLC, but this seems to be compensated by the excellent conductivity of the Pd-CeO_2/OLC (i.e., reduced band gap of 0.176 versus 0.433 eV). Also, Pd-CeO_2/OLC shows the weakest adsorption for OH^* (−10.135 eV) compared to Pd/OLC (−10.448 eV) and Pd/CB (−13.116 eV). The weak adsorption energy between the OH^* and Pd-CeO_2/OLC confirms that CeO_2 is an efficient oxygen storage promoter,[39] which can speedily supply enough OH species as needed for the fast kinetics of the EOR. In addition, the bulky nature of the CeO_2 may create some steric hindrance to the Pd, thereby mitigating the risk of poisoning the active Pd species.

Figure 9 compares the band structures of Pd-CeO_2/OLC, Pd/OLC, and Pd/CB, and their corresponding partial densities of states (PDOS). The available states increase as follows: Pd/C < Pd/OLC < Pd-CeO_2/OLC, with Pd-CeO_2/OLC having the highest. The Pd-CeO_2/OLC shows the highest value and the closest PDOS to the Fermi level. The increase in PDOS (orbitals) is an indication of the enhanced movement of electrons within the structure (i.e., enhanced electronic conductivity), which explains why Pd-CeO_2/OLC shows the best DFT energy band gap (0.176 eV), followed by Pd/OLC (0.433 eV) and Pd/C (0.582 eV). The smaller band gap for Pd-CeO_2/OLC further eases the movement of electrons from the valence band to the conduction band. In spite of Pd/OLC and Pd-CeO_2/OLC having similar d orbital electrons' contribution, the superior conductivity recorded for Pd/CeO_2/OLC is attributed to the increase of electronic density resulting from the 2p-orbital of CeO_2, which is about four times larger than those observed for both Pd/C and Pd/OLC.

In addition to the DFT data, it can be observed that both HRTEM and XPS data provide further insights into the reasons for the enhanced performance of Pd-CeO_2/OLC toward EOR (Figure 10). First, HRTEM shows intimate association of the Pd with CeO_2, confirming the interfacial

https://doi.org/10.1021/acsomega.3c04427
ACS Omega 2024, 9, 7439−7451

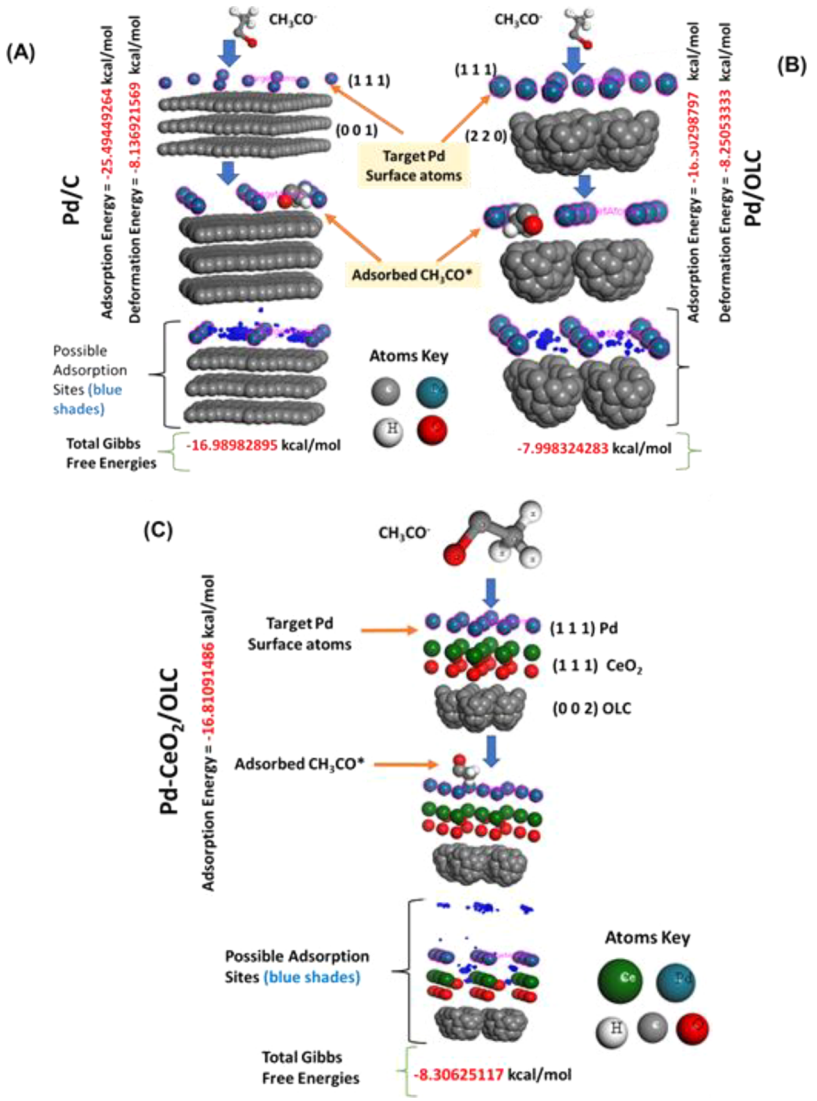

Figure 8. Acetyl group adsorption sites at the surfaces of (A) Pd/CB, (B) Pd/OLC, and (C) Pd-CeO_2/OLC. The dark blue shaded dots show the possible sites where ethanol molecules are adsorbed.

interaction between the two species (see Figure 10 A). Notably, the interfacial interaction of Pd-CeO_2/OLC occurs with the attachment of the {111} facet of CeO_2 directly on the {200} and {111} facets of Pd, which is more significant at the higher facet of Pd than the lower facet. Regarding XPS, it has been reported that XPS data show Pd^{2+}/Pd^0 and Ce^{4+}/Ce^{3+} redox couples interact to keep Pd in its ionic state while at the same time allowing the availability of the lattice oxygen for the EOR.[11] In the solid solution of $Ce_{1-x}Pd_xO_{2-\delta}$, it is either that the Ce^{4+} is reduced to Ce^{3+} or the Pd^{2+} is reduced to Pd^0, or both. However, considering that the electronic configuration of Pd^{2+} ($4d^8$ $5s^0$) means that there is a vacancy in its valence band, coupled with the fact that it lies below the Ce^{4+}4f band, it simply means that it should be preferentially reduced to Pd(0) rather than Ce^{4+} to Ce^{3+}. The formation of Pd(0) means that the Pd valence will cross the Ce^{4+} level toward the Fermi level since the addition of electrons tends to move the electronic states much closer to the Fermi energy level.[9] From the XPS data obtained in this work, the Pd-CeO_2/OLC shows slightly higher binding energy of the Pd 3d core energy (i.e., Pd(0) $3d_{5/2}$ at 335.2 eV and Pd(II) $3d_{3/2}$ at 340.4 eV) compared to the Pd/OLC (i.e., Pd(0) $3d_{5/2}$ at 335.0 eV and Pd(II) $3d_{3/2}$ at 340.0 eV), indicating effective charge and the formation of a stable $Ce_{1-x}Pd_xO_{2-\delta}$ for the Pd-CeO_2/OLC.[9]

Importantly, from the valence band spectra of the catalysts, the d-bandwidth increases as Pd/CB (1.04 eV) < Pd/OLC (3.26 eV) < Pd-CeO_2/OLC (9.00 eV) (Figures 10B–D). Similarly, the d-band center (ε_d) is shifted downward relative to the Fermi level, i.e., Pd/CB (3.2 eV) < Pd/OLC (3.6 eV) < Pd-CeO_2/OLC (4.2 eV). The broadening of the d-band is indicative of increased compressive strain on the Pd lattice, which leads to an increase in the overlap of the electronic states between the metal atoms (in this case, the Pd and Ce). This phenomenon has been observed by other workers too.[40] It is well established in various articles that the positive shift of the Pd 3D core-level and the downshifting d-band center result from electron loss. In fact, the downshifting d-band center is generally considered highly important as it suggests a weaker adsorption of the adsorbing species on the catalyst's surface (as also predicted by the DFT for both the OLC-based catalysts, Table S4), which, of course, is the result of reduced electron back-donation from the surface of the metals to the antibonding level of the adsorbed species.[41,42]

https://doi.org/10.1021/acsomega.3c04427
ACS Omega 2024, 9, 7439−7451

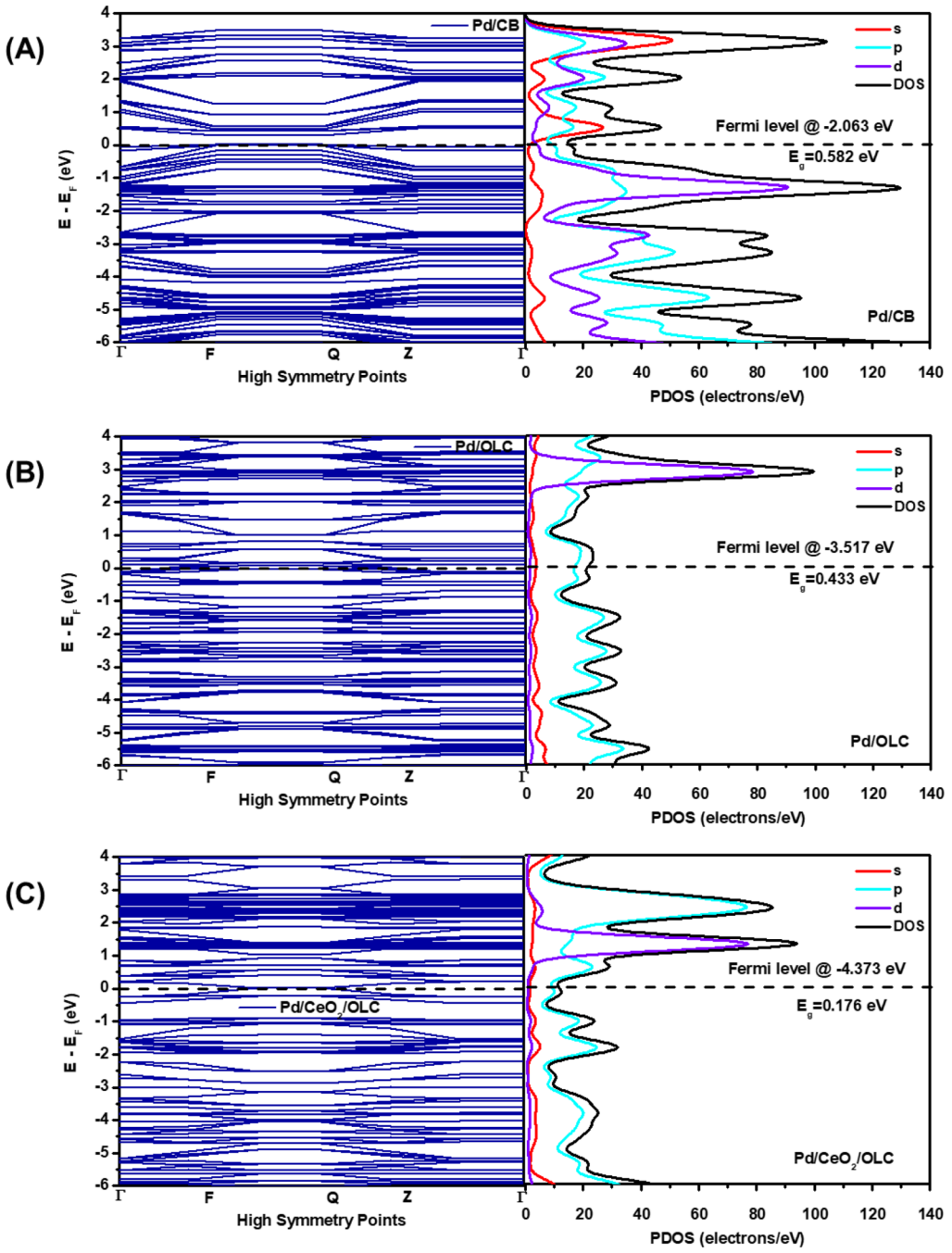

Figure 9. Band structure and corresponding partial density of states (PDOS) of (A) Pd/C, (B) Pd/OLC, and (C) Pd-CeO_2/OLC.

In summary, the modulation of the electronic merit of the Pd-OLC by CeO_2, evident by the enhanced interfacial interaction between the Pd and CeO_2, increased lattice strain, and downshifting d-band center, resulted in enhanced electrocatalytic EOR, ADEFC, and ethanol sensors. Therefore, the enhanced electrocatalysis of EOR by the Pd-CeO_2/OLC is the result of the robust interfacial interaction of the Pd with CeO_2/OLC. Experiments and theoretical studies prove that, unlike carbon black, the OLC exhibits strong positive impacts on the electronic states of the Pd-CeO_2, enhancing the electrocatalytic performance of the Pd-CeO_2/OLC.

4. CONCLUSIONS

This research reports the experimental and theoretical investigation of the interfacial interaction among Pd nanocrystals on supports (CB, OLC, and CeO_2/OLC) (i.e., Pd/CB, Pd/OLC, and Pd-CeO_2/OLC) toward ADEFC and ethanol sensors. The fabrication of porous Pd-CeO_2/OLC nanocrystals follows sol−gel and impregnation methods. As-prepared Pd-CeO_2/OLC exhibits considerably high peak power density (P_{max} = 27.15 mW cm^{-2}) in the membrane-free micro 3D-printed ADEFC that is 1.38- and 7.58- times those of Pd/OLC (19.72 mW cm^{-2}) and Pd/CB (3.59 mW cm^{-2}), respectively, in addition to superb stability for 48 h. This is owing to the exceptional interfacial interaction among Pd, CeO_2, and OLC, proved by the DFT studies that facilitates the modulation of

https://doi.org/10.1021/acsomega.3c04427
ACS Omega 2024, 9, 7439−7451

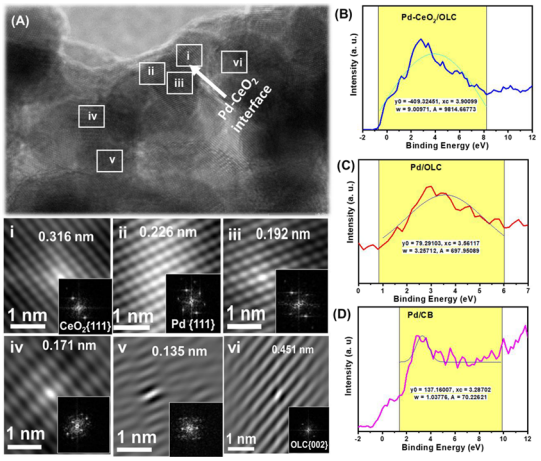

Figure 10. (A) HRTEM showing the interfacial interaction between Pd and CeO_2 in Pd-CeO_2/OLC with Fast Fourier Transform (FFT) of Pd-CeO_2/OLC (i-vi), and the valence band spectra of the (B) Pd-CeO_2/OLC, (C) Pd/OLC, and (D) Pd/CB catalysts.

the d-band center of Pd and the ease of formation of active oxygenated species by the CeO_2 needed for ADEFCs. Also, Pd-CeO_2/OLC delivers impressive ethanol sensitivity (0.00024 mA mM^{-1}) and limit of detection (LoD = 8.7 mM) and acceptable recoveries (89−108%) of commercial alcoholic beverages (i.e., human serum, Amstel beer, and Nederberg Wine). This study shows the potential of Pd-CeO_2/OLC in ethanol fuel and real samples of commercial alcoholic beverages and human serum.

■ ASSOCIATED CONTENT

Supporting Information

The Supporting Information is available free of charge at https://pubs.acs.org/doi/10.1021/acsomega.3c04427.

TEM, nanoparticle size distribution, and HRTEM; BET surface areas and porosity data; EDX data; CVs, plots of peak currents versus square root of scan rates; FTIR of EOR products; comparison of activities with literature; electrochemical sensing data of ethanol in human serum and commercial beer and wine; and DFT calculations of adsorbates with electrocatalysts (PDF)

■ AUTHOR INFORMATION

Corresponding Authors

Kamel Eid − *Gas Processing Center (GPC), College of Engineering, Qatar University, Doha 2713, Qatar;* orcid.org/0000-0001-5327-2497; Email: kamel.eid@qu.edu.qa

Daniel M. Wamwangi − *School of Physics, University of the Witwatersrand, Johannesburg 2050, South Africa;* Email: Daniel.Wamwangi@wits.ac.za

Kenneth I. Ozoemena − *School of Chemistry, Molecular Sciences Institute, University of the Witwatersrand, Johannesburg 2050, South Africa; State Key Laboratory of Advanced Technology for Materials Synthesis and Processing, School of Materials Science and Engineering, Wuhan University of Technology, Wuhan 430070, China;* orcid.org/0000-0001-7107-7003; Email: kenneth.ozoemena@wits.ac.za

Authors

Jimodo J. Ogada − *School of Chemistry, Molecular Sciences Institute and School of Physics, University of the Witwatersrand, Johannesburg 2050, South Africa*

Tobechukwu J. Ehirim − *School of Chemistry, Molecular Sciences Institute, University of the Witwatersrand, Johannesburg 2050, South Africa*

Adewale K. Ipadeola − *School of Chemistry, Molecular Sciences Institute, University of the Witwatersrand, Johannesburg 2050, South Africa; Gas Processing Center (GPC), College of Engineering and Center for Advanced Materials, Qatar University, Doha 2713, Qatar;* orcid.org/0000-0001-8896-6763

Aderemi B. Haruna − *School of Chemistry, Molecular Sciences Institute, University of the Witwatersrand, Johannesburg 2050, South Africa*

Patrick V. Mwonga − *School of Chemistry, Molecular Sciences Institute, University of the Witwatersrand, Johannesburg 2050, South Africa*

Aboubakr M. Abdullah − *Center for Advanced Materials, Qatar University, Doha 2713, Qatar*

Xiao-Yu Yang − *School of Chemistry, Molecular Sciences Institute, University of the Witwatersrand, Johannesburg 2050, South Africa; State Key Laboratory of Advanced Technology for Materials Synthesis and Processing, School of Materials Science and Engineering, Wuhan University of Technology, Wuhan 430070, China;* orcid.org/0000-0002-0880-9790

Complete contact information is available at: https://pubs.acs.org/10.1021/acsomega.3c04427

Author Contributions

#J.J.O. and T.J.E. contributed equally to the work.

Notes

The authors declare no competing financial interest.

■ ACKNOWLEDGMENTS

The authors are grateful for the financial support of the National Foundation of Research (NRF), the Department of Science and Innovation (DSI), and the University of the Witwatersrand (Wits) through the DSI-NRF-Wits SARChI Chair in Materials Electrochemistry and Energy Technologies (MEET) (UID No.: 132739). J.J.O. thanks the NRF for both MSc and Doctoral scholarships. We thank the CHPC (Cape Town, South Africa) for granting us unrestricted access to the computing facilities for DFT calculations. We thank the University of the Witwatersrand for paying the Open Access fee for this article.

■ REFERENCES

(1) Chu, M.; Yang, H.; Ye, X.; Qiu, Y.; Cao, M.; Chen, J.; Yuan, X.; Zhang, Q. Controllable Construction of PtBi Nanostructures for Enhanced Ethanol Oxidation in Acidic Media. *J. Phys. Chem. C* **2023**, *127* (17), 8062−8070.

(2) Wu, F.; Eid, K.; Abdullah, A. M.; Niu, W.; Wang, C.; Lan, Y.; Elzatahry, A. A.; Xu, G. Unveiling one-pot template-free fabrication of exquisite multidimensional PtNi multicube nanoarchitectonics for the efficient electrochemical oxidation of ethanol and methanol with a great tolerance for CO. *ACS Appl. Mater. Interfaces* **2020**, *12* (28), 31309−31318.

(3) Badwal, S.; Giddey, S.; Kulkarni, A.; Goel, J.; Basu, S. Direct ethanol fuel cells for transport and stationary applications−A comprehensive review. *Appl. Energy* **2015**, *145*, 80−103.

(4) Tyree, D. J.; Huntington, P.; Holt, J.; Ross, A. L.; Schueler, R.; Petkie, D. T.; Kim, S. S.; Grigsby, C. C.; Neese, C.; Medvedev, I. R. Terahertz Spectroscopic Molecular Sensor for Rapid and Highly Specific Quantitative Analytical Gas Sensing. *ACS Sens.* **2022**, *7* (12), 3730−3740.
(5) Joseph, J. A.; Akkermans, S.; Van Impe, J. F. Processing Method for the Quantification of Methanol and Ethanol from Bioreactor Samples Using Gas Chromatography−Flame Ionization Detection. *ACS Omega* **2022**, *7* (28), 24121−24133.
(6) Nascimento, E. P.; Firmino, H. C.; Santos, A. M.; Sales, H. B.; Silva, V. D.; Macedo, D. A.; Neves, G. A.; Medeiros, E. S.; Menezes, R. R. Facile synthesis of hollow F-doped SnO2 nanofibers and their efficiency in ethanol sensing. *J. Am. Ceram. Soc.* **2021**, *104* (3), 1297−1308.
(7) Ipadeola, A. K.; Haruna, A. B.; Abdullah, A. M.; Shibl, M. F.; Ahmadalie, D.; Ozoemena, K. I.; Eid, K. Electrocatalytic CO Oxidation on Porous Ternary PdNiO-CeO2/Carbon Black Nanocatalysts: Effect of Supports and Electrolytes. *Catal. Today* **2023**, *421*, No. 114178.
(8) Guo, J.; Huang, R.; Li, Y.; Yu, Z.; Wan, L.; Huang, L.; Xu, B.; Ye, J.; Sun, S. Surface structure effects of high-index faceted Pd nanocrystals decorated by Au submonolayer in enhancing the catalytic activity for ethanol oxidation reaction. *J. Phys. Chem. C* **2019**, *123* (38), 23554−23562.
(9) Hegde, M. S.; Bera, P. Noble metal ion substituted CeO2 catalysts: Electronic interaction between noble metal ions and CeO2 lattice. *Catal. Today* **2015**, *253*, 40−50.
(10) Ipadeola, A. K.; Haruna, A. B.; Abdullah, A. M.; Al-Hajri, R. S.; Viter, R.; Ozoemena, K. I.; Eid, K. Ternary PdNiO nanocrystals-ornamented porous CeO 2/onion-like carbon for electrooxidation of carbon monoxide: unveiling the effect of supports and electrolytes. *Catal. Sci. Technol.* **2023**, *13* (10), 3035−3045.
(11) Sharma, S.; Mukri, B. D.; Hegde, M. S. Direct evidence of redox interaction between metal ion and support oxide in Ce(0.98)-Pd(0.02)O(2-delta) by a combined electrochemical and XPS study. *Dalton Trans.* **2011**, *40* (43), 11480−11489.
(12) Ogada, J. J.; Ipadeola, A. K.; Mwonga, P. V.; Haruna, A. B.; Nichols, F.; Chen, S.; Miller, H. A.; Pagliaro, M. V.; Vizza, F.; Varcoe, J. R.; Meira, D. M.; Wamwangi, D. M.; Ozoemena, K. I. CeO_2 Modulates the Electronic States of a Palladium Onion-Like Carbon Interface into a Highly Active and Durable Electrocatalyst for Hydrogen Oxidation in Anion-Exchange-Membrane Fuel Cells. *ACS Catal.* **2022**, *12* (12), 7014−7029.
(13) Miller, H. A.; Vizza, F.; Marelli, M.; Zadick, A.; Dubau, L.; Chatenet, M.; Geiger, S.; Cherevko, S.; Doan, H.; Pavlicek, R. K.; et al. Highly active nanostructured palladium-ceria electrocatalysts for the hydrogen oxidation reaction in alkaline medium. *Nano Energy* **2017**, *33*, 293−305.
(14) Hantel, M.; Presser, V.; McDonough, J.; Feng, G.; Cummings, P. T.; Gogotsi, Y.; Kötz, R. In situ electrochemical dilatometry of onion-like carbon and carbon black. *J. Electrochem. Soc.* **2012**, *159* (11), A1897.
(15) Ipadeola, A. K.; Eid, K.; Abdullah, A. M.; Ozoemena, K. I. Pd-Nanoparticles Embedded Metal−Organic Framework-Derived Hierarchical Porous Carbon Nanosheets as Efficient Electrocatalysts for Carbon Monoxide Oxidation in Different Electrolytes. *Langmuir* **2022**, *38* (36), 11109−11120.
(16) Pointecouteau, R.; Florian, P.; Rodriguez, V.; Bion, N.; Demourgues, A. Unveiling structural defects by 139La NMR and Raman spectroscopies at the origin of surface stability for the design of cerium-based catalysts. *J. Phys. Chem. C* **2023**, *127* (6), 3020−3031.
(17) Loridant, S. Raman spectroscopy as a powerful tool to characterize ceria-based catalysts. *Catal. Today* **2021**, *373*, 98−111.
(18) Venkataswamy, P.; Damma, D.; Jampaiah, D.; Mukherjee, D.; Vithal, M.; Reddy, B. M. Cr-doped CeO2 nanorods for CO oxidation: insights into promotional effect of Cr on structure and catalytic performance. *Catal. Lett.* **2020**, *150* (4), 948−962.
(19) Chen, S.; Li, S.; You, R.; Guo, Z.; Wang, F.; Li, G.; Yuan, W.; Zhu, B.; Gao, Y.; Zhang, Z.; et al. Elucidation of Active Sites for CH4 Catalytic Oxidation over Pd/CeO2 Via Tailoring Metal−Support Interactions. *ACS Catal.* **2021**, *11* (9), 5666−5677.
(20) Wang, J.; Li, B.; Yersak, T.; Yang, D.; Xiao, Q.; Zhang, J.; Zhang, C. Recent advances in Pt-based octahedral nanocrystals as high performance fuel cell catalysts. *J. Mater. Chem. A* **2016**, *4* (30), 11559−11581.
(21) Jain, S.; Shah, J.; Negi, N. S.; Sharma, C.; Kotnala, R. K. Significance of interface barrier at electrode of hematite hydroelectric cell for generating ecopower by water splitting. *Int. J. Energy Res.* **2019**, *43* (9), 4743−4755.
(22) Zhang, X.; Qin, J.; Xue, Y.; Yu, P.; Zhang, B.; Wang, L.; Liu, R. Effect of aspect ratio and surface defects on the photocatalytic activity of ZnO nanorods. *Sci. Rep.* **2014**, *4* (1), 4596.
(23) Park, J. H.; Alshammari, F. H.; Wang, Z.; Alshareef, H. N. Interface Engineering for Precise Threshold Voltage Control in Multilayer-Channel Thin Film Transistors. *Adv. Mater. Interfaces* **2016**, *3* (24), No. 1600713.
(24) Ozoemena, K. I.; Mathebula, N. S.; Pillay, J.; Toschi, G.; Verschoor, J. A. Electron transfer dynamics across self-assembled N-(2-mercaptoethyl) octadecanamide/mycolic acid layers: impedimetric insights into the structural integrity and interaction with anti-mycolic acid antibodies. *Phys. Chem. Chem. Phys.* **2010**, *12* (2), 345−357.
(25) Mofokeng, T. P.; Ipadeola, A. K.; Tetana, Z. N.; Ozoemena, K. I. Defect-Engineered Nanostructured Ni/MOF-Derived Carbons for an Efficient Aqueous Battery-Type Energy Storage Device. *ACS Omega* **2020**, *5* (32), 20461−20472.
(26) Hassan, K. M.; Hathoot, A. A.; Maher, R.; Abdel Azzem, M. Electrocatalytic oxidation of ethanol at Pd, Pt, Pd/Pt and Pt/Pd nano particles supported on poly 1,8-diaminonaphthalene film in alkaline medium. *RSC Adv.* **2018**, *8* (28), 15417−15426.
(27) Lv, J.-J.; Wisitruangsakul, N.; Feng, J.-J.; Luo, J.; Fang, K.-M.; Wang, A.-J. Biomolecule-assisted synthesis of porous PtPd alloyed nanoflowers supported on reduced graphene oxide with highly electrocatalytic performance for ethanol oxidation and oxygen reduction. *Electrochim. Acta* **2015**, *160*, 100−107.
(28) Fu, S.; Zhu, C.; Du, D.; Lin, Y. Facile one-step synthesis of three-dimensional Pd−Ag bimetallic alloy networks and their electrocatalytic activity toward ethanol oxidation. *ACS Appl. Mater. Interfaces* **2015**, *7* (25), 13842−13848.
(29) Liang, Y.-Y.; Qiang, W.; Liang, F. Analysis of Catalytic Activity of Au@ Pd Core-Shell Nanodendrites for Highly Efficient Ethanol Electrooxidation. *Chin. J. Anal. Chem.* **2021**, *49* (5), e21087−e21095.
(30) Li, S.; Guan, A.; Wang, H.; Yan, Y.; Huang, H.; Jing, C.; Zhang, L.; Zhang, L.; Zheng, G. Hybrid palladium nanoparticles and nickel single atom catalysts for efficient electrocatalytic ethanol oxidation. *J. Mater. Chem. A* **2022**, *10* (11), 6129−6133.
(31) Ipadeola, A. K.; Lisa Mathebula, N. Z.; Pagliaro, M. V.; Miller, H. A.; Vizza, F.; Davies, V.; Jia, Q.; Marken, F.; Ozoemena, K. I. Unmasking the Latent Passivating Roles of Ni (OH) 2 on the Performance of Pd−Ni Electrocatalysts for Alkaline Ethanol Fuel Cells. *ACS Appl. Energy Mater.* **2020**, *3* (9), 8786−8802.
(32) Liang, Z.; Zhao, T.; Xu, J.; Zhu, L. Mechanism study of the ethanol oxidation reaction on palladium in alkaline media. *Electrochim. Acta* **2009**, *54* (8), 2203−2208.
(33) Hibbitts, D. D.; Neurock, M. Influence of oxygen and pH on the selective oxidation of ethanol on Pd catalysts. *J. Catal.* **2013**, *299*, 261−271.
(34) Monyoncho, E. A.; Steinmann, S. N.; Michel, C.; Baranova, E. A.; Woo, T. K.; Sautet, P. Ethanol electro-oxidation on palladium revisited using polarization modulation infrared reflection absorption spectroscopy (PM-IRRAS) and density functional theory (DFT): why is it difficult to break the C−C bond? *ACS Catal.* **2016**, *6* (8), 4894−4906.
(35) Li, M.; Guo, W.; Jiang, R.; Zhao, L.; Shan, H. Decomposition of ethanol on Pd (111): a density functional theory study. *Langmuir* **2010**, *26* (3), 1879−1888.
(36) Miao, B.; Wu, Z.-P.; Xu, H.; Zhang, M.; Chen, Y.; Wang, L. DFT studies on the key competing reaction steps towards complete

https://doi.org/10.1021/acsomega.3c04427
ACS Omega 2024, 9, 7439−7451

ethanol oxidation on transition metal catalysts. *Comput. Mater. Sci.* **2019**, *156*, 175−186.
(37) Yang, T.; Yang, S.; Jin, W.; Zhang, Y.; Barsan, N.; Hemeryck, A.; Wageh, S.; Al-Ghamdi, A. A.; Liu, Y.; Zhou, J.; et al. Density Functional Investigation on alpha-MoO3 (100): Amines Adsorption and Surface Chemistry. *ACS Sens.* **2022**, *7* (4), 1213−1221.
(38) Wang, P.; Yuan, X.; Cui, Z.; Xu, C.; Sun, Z.; Li, J.; Liu, J.; Tian, Y.; Li, H. A Nanometer-Sized Graphite/Boron-Doped Diamond Electrochemical Sensor for Sensitive Detection of Acetaminophen. *ACS Omega* **2021**, *6* (9), 6326−6334.
(39) Yuan, Q.; Duan, H. H.; Li, L. L.; Sun, L. D.; Zhang, Y. W.; Yan, C. H. Controlled synthesis and assembly of ceria-based nanomaterials. *J. Colloid Interface Sci.* **2009**, *335* (2), 151−167.
(40) Hu, S.; Scudiero, L.; Ha, S. Electronic effect on oxidation of formic acid on supported Pd−Cu bimetallic surface. *Electrochim. Acta* **2012**, *83*, 354−358.
(41) Zhao, J.; Zha, S.; Mu, R.; Zhao, Z.-J.; Gong, J. Coverage effect on the activity of the acetylene semihydrogenation over Pd−Sn catalysts: a density functional theory study. *J. Phys. Chem. C* **2018**, *122* (11), 6005−6013.
(42) Zhang, L.; Chen, R.; Tu, Y.; Gong, X.; Cao, X.; Xu, Q.; Li, Y.; Ye, B.; Ye, Y.; Zhu, J. Revealing the Crystal Facet Effect of Ceria in Pd/CeO2 Catalysts toward the Selective Oxidation of Benzyl Alcohol. *ACS Catal.* **2023**, *13* (4), 2202−2213.

https://doi.org/10.1021/acsomega.3c04427
ACS Omega 2024, 9, 7439−7451